



## Correlation of in-situ transmission electron microscopy and microchemistry analysis of radiation-induced precipitation and segregation in ion irradiated advanced ferritic/martensitic steels

Ce Zheng<sup>a,\*</sup>, Jia-Hong Ke<sup>b,1</sup>, Stuart A. Maloy<sup>c</sup>, Djamel Kaoumi<sup>a</sup>

<sup>a</sup> Department of Nuclear Engineering, North Carolina State University, Raleigh, NC, USA

<sup>b</sup> Department of Materials Science and Engineering, University of Wisconsin-Madison, Madison, WI, USA

<sup>c</sup> Materials Science & Technology Division, Los Alamos National Laboratory, Los Alamos, NM, USA

### ARTICLE INFO

#### Article history:

Received 16 October 2018

Accepted 14 December 2018

Available online xxxx

#### Keywords:

Ferritic/martensitic steels

Ion irradiation

In-situ transmission electron microscopy

Energy dispersive X-ray spectroscopy

Precipitation

### ABSTRACT

This article presents a novel method combining ion irradiation, in-situ transmission electron microscopy (TEM), and microchemistry analysis before/after irradiation, which allows to examine same microstructural areas throughout ion irradiation. A 12 wt% Cr Ferritic/Martensitic steel (HT9) was irradiated in the TEM to  $1.17 \times 10^{20}$  ions·m<sup>-2</sup> at 440 °C using 1 MeV Kr<sup>2+</sup> ions, and the in-situ characterization focused on radiation-induced precipitation and segregation. Results of in-situ experiments were compared with those obtained from ex-situ experiments, to showcase how this method helps to better understand precipitation kinetics in the irradiated material examined ex-situ, for which only snapshots are available at limited doses.

© 2018 Published by Elsevier Ltd on behalf of Acta Materialia Inc.

Alloy HT9 is an advanced 12 wt% Cr Ferritic/Martensitic (F/M) steel. Compared with austenitic stainless steels currently used in light water reactors, alloy HT9 has a low thermal expansion coefficient, reasonable high temperature strength, and more importantly, better resistance to neutron induced swelling [1–3]. This alloy is thus considered as a promising candidate for core materials applications in Generation IV reactors and first wall and blankets for fusion reactors [4]. Nevertheless, neutron irradiation drives microstructural and microchemical evolutions in the material, inducing second-phase precipitation and segregation which can strongly degrade the mechanical properties of this alloy [5–8]. Recently, alloy HT9 has been widely investigated by ion irradiation [9–12] as ion irradiation works as a surrogate to emulate neutron irradiation in the appropriate reactor environment [13,14]. Whether irradiated with neutrons or ions, usually the irradiated bulk samples are examined ex-situ when the irradiation is over, and the samples are cooled down. Because of this, only snapshots of the microstructure at final doses reached at the end of irradiation are available. In contrast, coupling ion irradiation with in-situ transmission electron microscopy (TEM) can be powerful as it allows to characterize the evolution of

radiation-induced microstructures as a function of doses. Our previous studies of alloy HT9 and other F/M model alloys [15–17] have showed, by using this in-situ method, the size and number density of radiation-induced defects and the correlation of radiation-induced defects with pre-existing microstructures (e.g. grain boundaries, dislocations) can be followed as the damage proceeds. In this article, we present a novel method combining ion irradiation, in-situ TEM observation, and microchemistry analysis before and after irradiation, which allows for examining same microstructural areas of alloy HT9 throughout ion irradiation. As an example, F/M steel HT9 was irradiated in the TEM to 20 dpa at 440 °C using 1 MeV Kr<sup>2+</sup> ions, and the in-situ characterization focused on radiation-induced precipitation and segregation. Results of in-situ experiments are compared with those obtained from ex-situ experiments, to showcase how this method helps to better understand precipitation kinetics in the irradiated material examined ex-situ, for which only snapshots are available at limited doses.

F/M steel HT9 (heat # 84425) was received from Los Alamos National Laboratory (LANL). Its nominal compositions are given in Table 1. The same material was used to construct the ACO-3 hexagonal duct in Fast Flux Test Facility (FFTF) [18]. Prior to irradiation, the steel HT9 was subjected to a heat treatment consisting of normalizing at 1065 °C for 30 min/air cooling followed by tempering 750 °C for 1 h/air cooling, which lead to a tempered martensitic structure. TEM specimens of HT9 were prepared using the Focused Ion Beam (FIB) lift-out technique. More details about sample preparation can be found in [15].

\* Corresponding author at: Department of Nuclear Engineering, North Carolina State University, 3140 Burlington Engineering Labs, Room 2137, Raleigh, NC 27695-7909, USA. E-mail address: [czheng7@ncsu.edu](mailto:czheng7@ncsu.edu) (C. Zheng).

<sup>1</sup> Present address: Department of Mechanical, Industrial, and Manufacturing Engineering, Oregon State University, Corvallis, OR, USA.

**Table 1**  
Chemical compositions (wt%) of HT9 (heat # 84425) provided by LANL.

	Fe	Cr	Mo	Ni	Mn	W	V	Si	C	P	N	S
LANL Bal.	11.8	1.03	0.51	0.5	0.5	0.33	0.21	0.21	0.008	0.01	0.003	

In-situ TEM observation combined with ion irradiation was carried out at the Intermediate Voltage Electron Microscope (IVEM) Facility at Argonne National Laboratory. The facility consists of a Hitachi 9000 NAR transmission electron microscope coupled with a 500 keV NEC implanter. The TEM specimen was irradiated in the microscope at  $440 \pm 5$  °C using 1 MeV  $\text{Kr}^{2+}$  ions with the ion beam incident at  $30^\circ$  from the electron beam and typically  $\sim 13\text{--}16^\circ$  from the specimen normal. The irradiation dose rate in displacement per atom per second ( $\text{dpa}\cdot\text{s}^{-1}$ ) was estimated using the software package SRIM-2008 [19] under the “Kinchin-Pease” (a.k.a. quick damage) calculation mode. The measured ion flux of  $6.25 \times 10^{15}$  ions $\cdot\text{m}^{-2}\cdot\text{s}^{-1}$ , the nominal density of  $7.86 \times 10^3$  kg $\cdot\text{m}^{-3}$  and the displacement energy of 40 eV/atom [20] for metallic elements were used. As shown in Fig. 1, the damage profile of 1 MeV  $\text{Kr}^{2+}$  ions in HT9 is relatively uniform through the first 100 nm of the total range of 500 nm, resulting in an irradiation dose rate of  $\sim 1.07 \times 10^{-3}$   $\text{dpa}\cdot\text{s}^{-1}$  in the first 100 nm depth (corresponding to the thickness of TEM specimens). In total, the specimen was subject to a total fluence of  $1.17 \times 10^{20}$  ions $\cdot\text{m}^{-2}$ , or about 20 dpa. Sequential TEM bright field (BF) and corresponding dark field (DF) images were taken at the same area by tilting the sample holder accordingly to maintain consistent imaging conditions.

The microchemistry analysis before and after irradiation was performed on a FEI Titan 80-300 probe aberration corrected scanning/transmission electron microscope, at the Analytical Instrumentation Facility (AIF) at North Carolina State University. The microscope contains a high-brightness Schottky field emission electron source and four high counting rate Bruker© energy-dispersive X-ray detectors, enabling qualitative chemical mapping of the elemental distribution. Radiation-induced precipitation and segregation were characterized using the elemental mapping (a.k.a “ChemiSTEM”) and high angle annular dark field (STEM-HAADF) imaging methods.

Pre-existing precipitates in as-received HT9 were identified as (Cr, Mn)-rich carbides and V-rich nitrides. The carbides were found to mostly form at prior austenite grain boundaries (PAGBs) and lath grain boundaries. Besides, no other precipitates are observed in the as-received condition [11]. Fig. 2(a–b) shows STEM-HAADF micrographs and corresponding elemental maps of Ni and Si which were collected at the same area of alloy HT9 before and after irradiation, respectively.

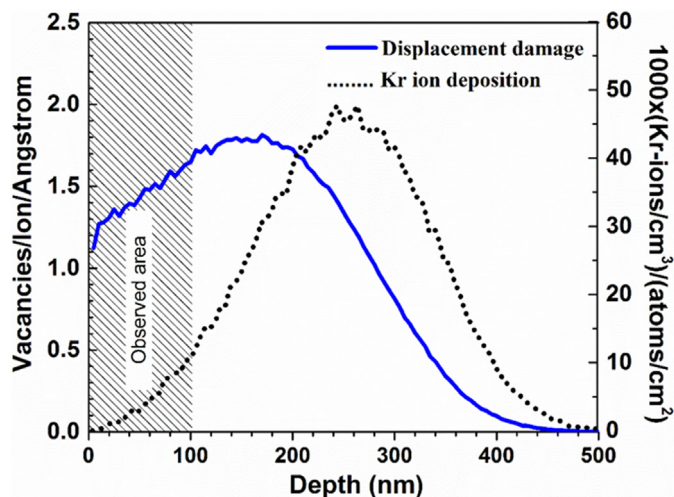
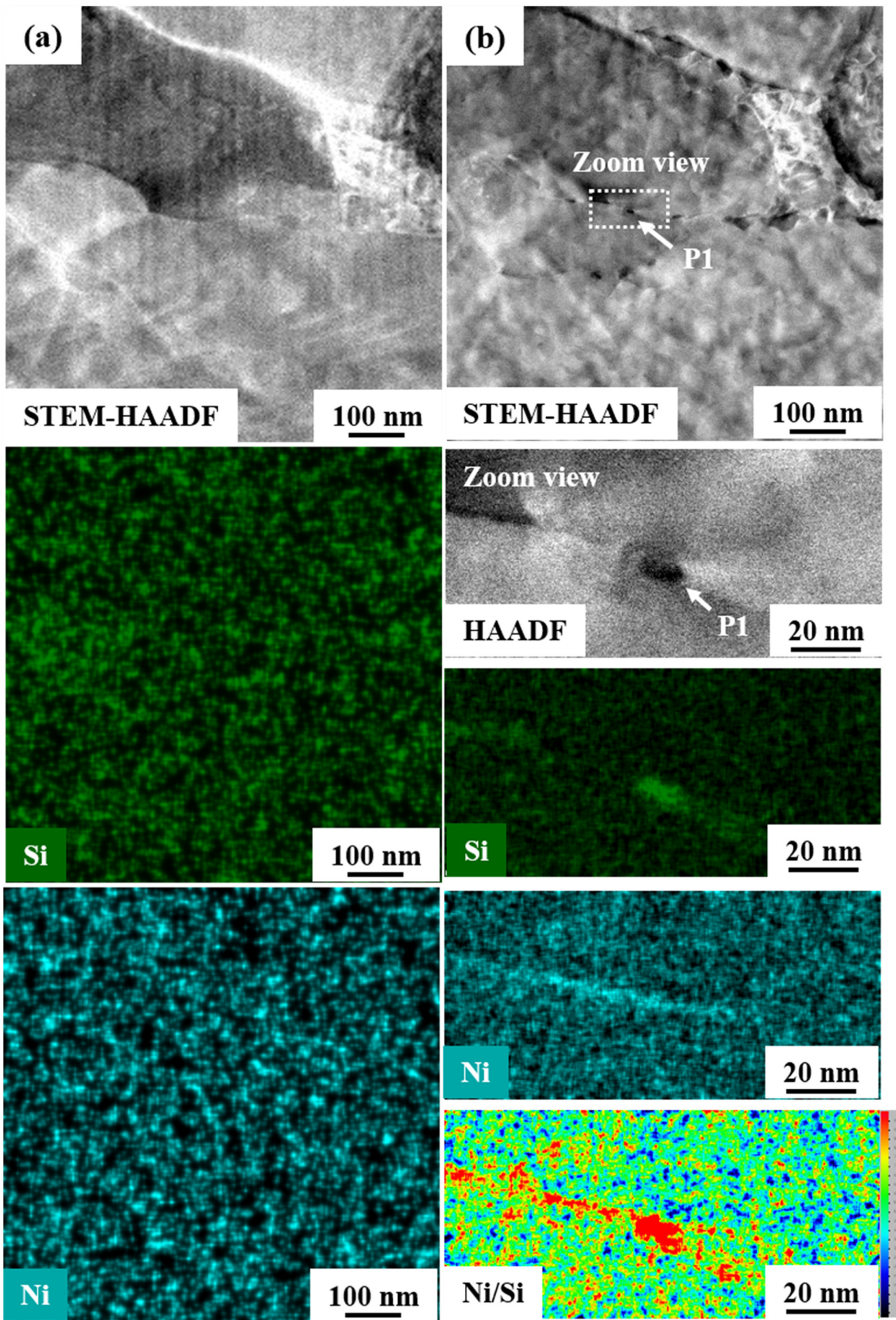


**Fig. 1.** SRIM-2008 calculations showing the damage profile and retention of Kr ions vs. depth in HT9 irradiated with 1 MeV  $\text{Kr}^{2+}$  ions. (one column wide).

Compared with the HAADF image taken before irradiation (Fig. 2(a)), new irregular features with dark contrasts are observed at grain boundaries in the HAADF image taken after irradiation (Fig. 2(b)). Since the HAADF imaging is highly sensitive to atomic number contrast (Z-contrast), the additional dark contrasts observed in Fig. 2(b) indicate second phase precipitates have formed during irradiation. The overlapping maps of Ni and Si further reveal the feature labeled as P1 in Fig. 2(b) is a Ni/Si-rich precipitate heterogeneously nucleating at the grain boundary where Ni and Si are also segregate. Similarly, the HAADF imaging and ChemiSTEM mapping were performed on another grain boundary of alloy HT9 before and after irradiation. Elemental maps of Cr, Mn and C shown in Fig. 3(a–b) indicate two pre-existing (Cr, Mn)-rich carbides still remain after ion irradiation. Also, the zoom view of Fig. 3(b) reveals new precipitates form at the grain boundary and between the two pre-existing carbides. Elemental maps of Cr, Mn and C show these precipitates are (Cr, Mn)-rich carbides. The dynamic observation of precipitate evolution was obtained using the in-situ TEM observation. Fig. 4 shows sequential TEM BF and corresponding DF images which were taken at the same area throughout irradiation (0–20 dpa). The grain observed in Fig. 4 is the same as that shown in Fig. 3. Compared with the TEM BF image taken at 4 dpa, a new precipitate labeled as P2 is found to appear in the TEM BF image taken at 8 dpa. The appearance of the precipitate P2 is also highlighted as additional white contrasts are observed in the TEM DF images taken at 8–20 dpa. The precipitate P2 observed in Fig. 4 is further located in Fig. 3(b) and identified as a (Cr, Mn)-rich carbide. Furthermore, the strong Moiré fringes presenting in the TEM BF image taken at 20 dpa also indicate the formation of second phase precipitates.

For comparison purpose, the steel HT9 irradiated to the same dose at the same temperature using 5 MeV  $\text{Fe}^{2+}$  ions was examined ex-situ. Details of this ex-situ irradiation experiment can be found in [11]. For HT9 irradiated and examined ex-situ, it is not possible to determine whether any pre-existing carbides dissolve or any new carbides nucleate during irradiation. However, Figs. 3–4 of this in-situ study show carbides can form in HT9 during irradiation. It highlights the advantage of using this novel in-situ method. In addition, Supplementary Fig. 1 (please download and see the Appendix) shows the spatial distribution of Mn/Ni/Si-rich precipitates (MNSPs) in HT9 ex-situ irradiated to 20 dpa at 440 °C. The heterogeneous nucleation of MNSPs at lath grain boundaries observed in ex-situ irradiated HT9 is consistent with the observation of in-situ irradiated HT9 (Fig. 2). The thermodynamic state of the equilibrium bulk MNSPs (T3 phase) was evaluated by the Thermo-Calc© software using the TCAL3 database [21]. The nominal alloy compositions shown in Table 1 were considered. In this thermodynamic analysis, both T3 ( $\text{Mn}_6\text{Ni}_{16}\text{Si}_7$ , a.k.a. G-phase) and T6 ( $\text{Mn}(\text{Ni},\text{Si})_2$ ) phases were included in the calculation. Note that the T6 phase did not form and only the T3 phase was found to be stable. Supplementary Fig. 2 (please download and see the Appendix) shows the calculated phase fraction of the equilibrium bulk MNSPs (T3 phase) as a function of temperature. Without ion irradiation, MNSPs are not able to form at temperatures higher than 370 °C, as seen in Supplementary Fig. 2. The thermodynamic prediction suggests that the MNSPs observed in both in-situ and ex-situ ion irradiated HT9 at 440 °C are induced by irradiation. The experimental observations of both in-situ and ex-situ irradiated HT9 are in agreement with previous cluster dynamic simulations [22] which suggested MNSPs formed in F/M steels are primarily irradiation-induced and, in particular, both heterogeneous nucleation and radiation-induced segregation at defect sinks are necessary for the formation of MNSPs.

However, the discrepancies of MNSPs precipitation between in-situ and ex-situ irradiation experiments of HT9 still exist. In contrast to in-situ irradiated HT9 at 440 °C, Supplementary Fig. 1 also shows the intra-granular precipitation of MNSPs (i.e. inside martensitic laths) can occur in HT9 ex-situ irradiated at the same temperature. Moreover, the number density of MNSPs observed in ex-situ irradiated HT9 is significantly higher than that observed in in-situ irradiated



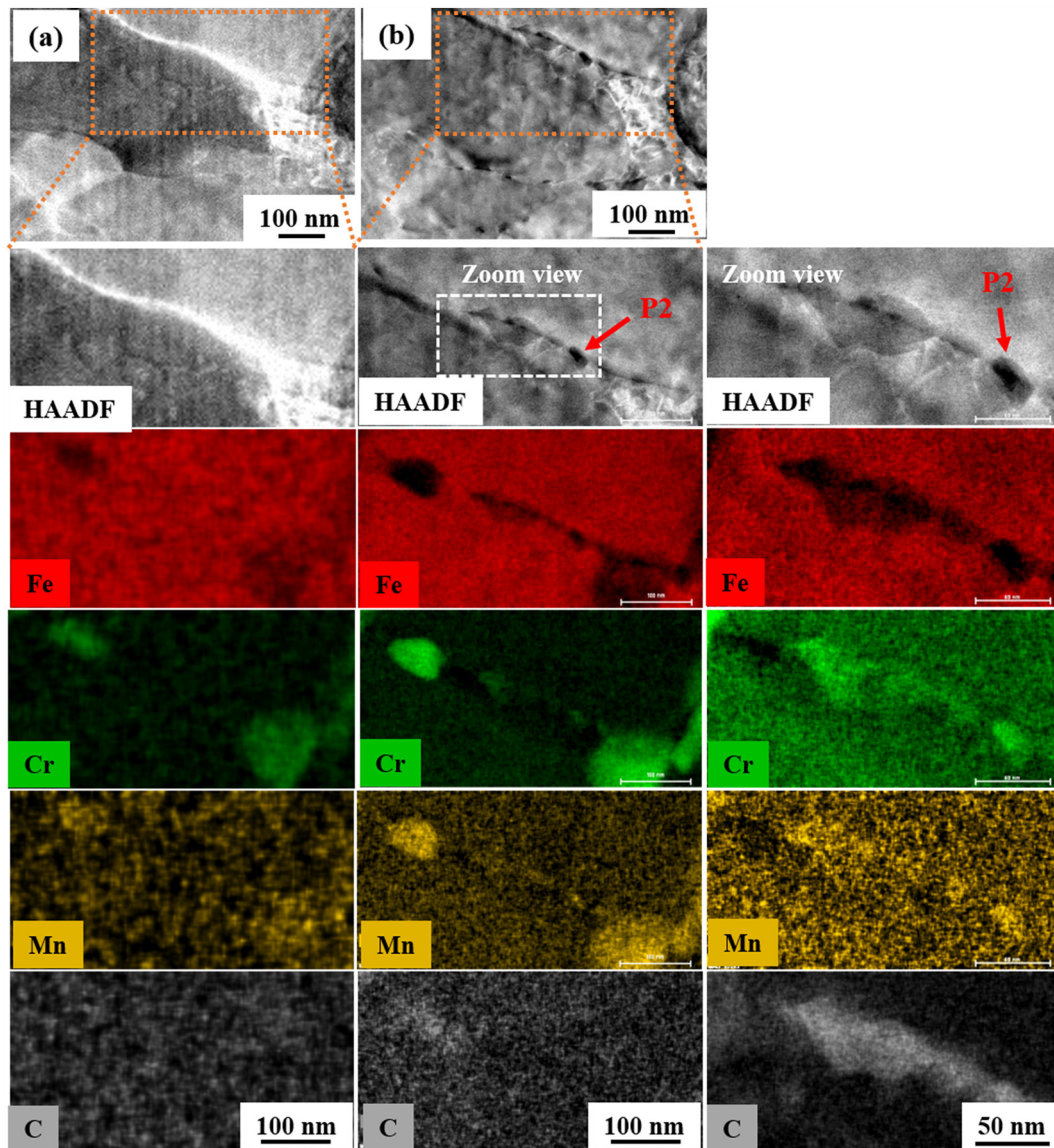


**Fig. 3.** STEM-HAADF micrographs and corresponding elemental maps of Fe, Cr, Mn and C were collected at the same area of HT9 (a) before and (b) after ion irradiation to 20 dpa at 440 °C. The zoom view of panel (b) highlights the formation of (Cr, Mn)-rich carbides at the grain boundary. One of these carbides (labeled as P2) is further observed in Fig. 4. (two columns wide).

HT9. The suppression of MNSPs precipitation can be explained by different mechanisms. First of all, free surfaces of the TEM thin foil specimen act as efficient sinks of point defects and thus somehow suppress defect-mediated diffusion of solutes toward other defect sinks (e.g. grain boundaries, dislocations). As a result, the local driving force of precipitate nucleation and growth decreases so that less precipitation can occur at these defect sinks. Such suppressed precipitation in thin sample parts has been reported in the study of high purity Fe-10 wt%Cr alloy implanted with  $\text{Al}^+$  and  $\text{O}^+$  ions at room temperature [23]. The suppressed precipitation of MNSPs may also be partially due to the decrease of dislocation loop density. In literature, in-situ TEM observations of HT9 irradiated to 20 dpa at 420–470 °C [15] showed the loss of radiation-induced dislocation loops followed by the build-up of dislocation network happened

with increasing dose, resulting in a decrease of dislocation loop density. Since dislocation loops can act as preferential nucleation sites for precipitation, the decrease of dislocation loop density suppresses the nucleation of MNSPs.

In conclusion, the novel in-situ method which combines ion irradiation, in-situ TEM observations, and microchemistry analysis before/after irradiation has proved to be a powerful tool for characterizing radiation-induced precipitation and segregation. Experiments using this in-situ method will allow for a better characterization and understanding of precipitation kinetics under irradiation compared to irradiated bulk samples examined ex-situ, where only snapshots are usually available at limited doses.

This work was a part of the NEUP-IRP project supported by the U.S. Department of Energy [grant number DE-NE0000639]. The access to

**Fig. 2.** STEM-HAADF micrographs and corresponding elemental maps of Ni and Si were collected at the same area of HT9 (a) before and (b) after ion irradiation to 20 dpa at 440 °C. The zoom view of panel (b) shows the formation of a Ni/Si-rich precipitate (labeled as P1) at the grain boundary where Ni and Si also segregate. (one column wide).

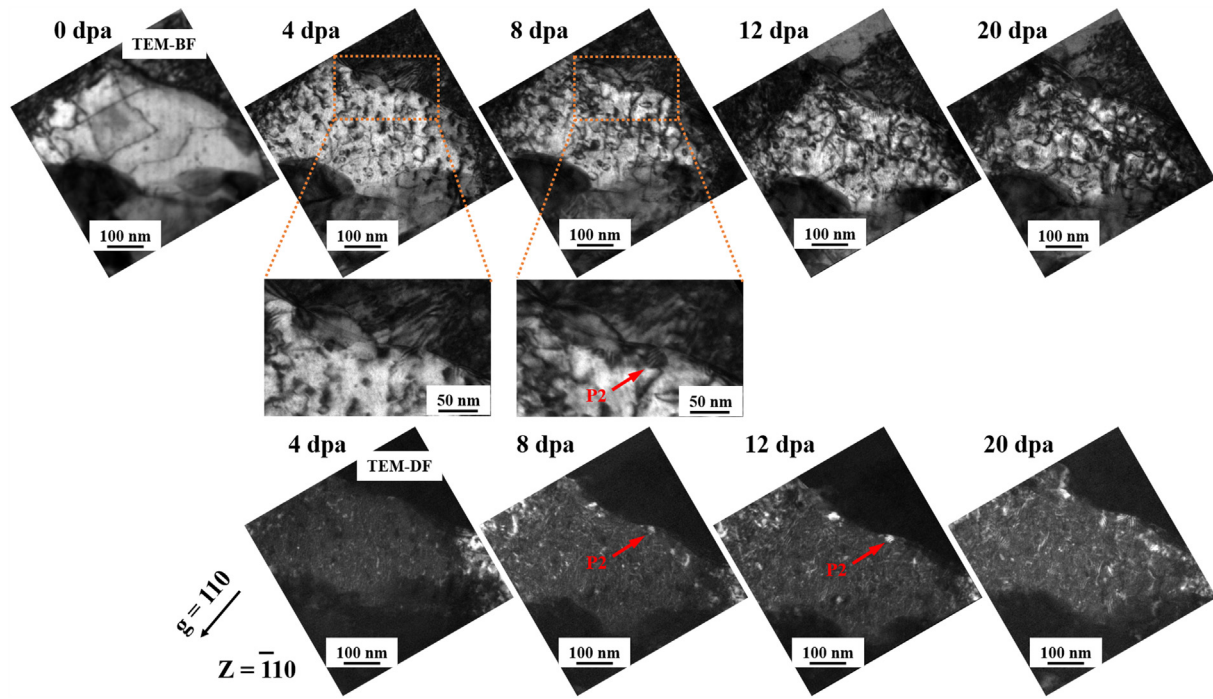


**Fig. 4.** In-situ TEM observation revealing the formation of a carbide (labeled as P2 in Fig. 3) occurring between 4 and 8 dpa at 440 °C. Sequential TEM-BF images also showing the evolution of dislocation loops formed under irradiation. (two columns wide).

the IVEM facility was through the Rapid Turnaround Experiment awarded by the Nuclear Science User Facilities [grant number FY17-1073]. The authors acknowledge Pete Baldo, Ed Ryan, Jing Hu, Meimei Li and Mark Kirk at the IVEM facility for their assistance. Sample preparation and ChemiSTEM characterization were carried out at the AIF facility. The AIF is supported by the State of North Carolina and the National Science Foundation [grant number ECCS-1542015], and is a member of the North Carolina Research Triangle Nanotechnology Network (RTNN), a site in the National Nanotechnology Coordinated Infrastructure (NNCI).

#### Appendix A. Supplementary data

Supplementary data to this article can be found online at <https://doi.org/10.1016/j.scriptamat.2018.12.018>.

#### References

- [1] F.A. Garner, R.J. Puigh, *J. Nucl. Mater.* 179–181 (1991) 577–580.
- [2] F.A. Garner, M.B. Toloczko, B.H. Sencer, *J. Nucl. Mater.* 276 (1) (2000) 123–142.
- [3] R.L. Klueh, A.T. Nelson, *J. Nucl. Mater.* 371 (1) (2007) 37–52.
- [4] S.J. Zinkle, G.S. Was, *Acta Mater.* 61 (3) (2013) 735–758.
- [5] T.S. Byun, M.B. Toloczko, T.A. Saleh, S.A. Maloy, *J. Nucl. Mater.* 432 (1) (2013) 1–8.
- [6] O. Anderoglu, J. Van den Bosch, P. Hosemann, E. Stergar, B.H. Sencer, D. Bhattacharyya, R. Dickerson, P. Dickerson, M. Hartl, S.A. Maloy, *J. Nucl. Mater.* 430 (1) (2012) 194–204.
- [7] B.H. Sencer, J.R. Kennedy, J.I. Cole, S.A. Maloy, F.A. Garner, *J. Nucl. Mater.* 414 (2) (2011) 237–242.
- [8] P. Dubuisson, D. Gilbon, J.L. Séran, *J. Nucl. Mater.* 205 (1993) 178–189.
- [9] E. Getto, K. Sun, A.M. Monterrosa, Z. Jiao, M.J. Hackett, G.S. Was, *J. Nucl. Mater.* 480 (2016) 159–176.
- [10] E. Getto, K. Sun, G.S. Was, *J. Nucl. Mater.* 485 (2017) 154–158.
- [11] C. Zheng, M.A. Auger, M.P. Moody, D. Kaoumi, *J. Nucl. Mater.* 491 (2017) 162–176.
- [12] C. Zheng, D. Kaoumi, *Mater. Charact.* 134 (2017) 152–162.
- [13] G.S. Was, Z. Jiao, E. Getto, K. Sun, A.M. Monterrosa, S.A. Maloy, O. Anderoglu, B.H. Sencer, M. Hackett, *Scr. Mater.* 88 (2014) 33–36.
- [14] S.J. Zinkle, L.L. Snead, *Scr. Mater.* 143 (2018) 154–160.
- [15] C. Zheng, S. Maloy, D. Kaoumi, *Philos. Mag.* 98 (26) (2018) 2440–2456.
- [16] D. Kaoumi, J. Adamson, *J. Nucl. Mater.* 448 (1–3) (2014) 233–238.
- [17] D. Kaoumi, J. Adamson, M. Kirk, *J. Nucl. Mater.* 445 (1–3) (2014) 12–19.
- [18] S.A. Maloy, M. Toloczko, J. Cole, T.S. Byun, *J. Nucl. Mater.* 415 (3) (2011) 302–305.
- [19] J.F. Ziegler, M.D. Ziegler, J.P. Biersack, *Nucl. Instrum. Methods Phys. Res., Sect. B* 268 (11) (2010) 1818–1823.
- [20] N. Juslin, K. Nordlund, J. Wallenius, L. Malerba, *Nucl. Instrum. Methods Phys. Res., Sect. B* 255 (1) (2007) 75–77.
- [21] J.O. Andersson, T. Helander, L. Höglund, P. Shi, B. Sundman, *Calphad* 26 (2) (2002) 273–312.
- [22] J.-H. Ke, H. Ke, G.R. Odette, D. Morgan, *J. Nucl. Mater.* 498 (2018) 83–88.
- [23] C. Zheng, A. Gentils, J. Ribis, O. Kaïtasov, V.A. Borodin, M. Descoins, D. Mangelinck, *Philos. Mag.* 94 (25) (2014) 2937–2955.